Bull Earthquake Eng
DOI 10.1007/s10518-008-9078-1

ORIGINAL RESEARCH PAPER

Numerical analyses of fault–foundation interaction

I. Anastasopoulos · A. Callerio · M. F. Bransby · M. C. R. Davies · A. El Nahas · E. Faccioli · G. Gazetas · A. Masella · R. Paolucci · A. Pecker · E. Rossignol

Received: 22 October 2007 / Accepted: 14 July 2008

Abstract Field evidence from recent earthquakes has shown that structures can be designed to survive major surface dislocations. This paper: (i) Describes three different finite element (FE) methods of analysis, that were developed to simulate dip slip fault rupture propagation through soil and its interaction with foundation–structure systems; (ii) Validates the developed FE methodologies against centrifuge model tests that were conducted at the University of Dundee, Scotland; and (iii) Utilises one of these analysis methods to conduct a short parametric study on the interaction of idealised 2- and 5-story residential structures lying on slab foundations subjected to normal fault rupture. The comparison between numerical and centrifuge model test results shows that reliable predictions can be achieved with reasonably sophisticated constitutive soil models that take account of soil softening after failure. A prerequisite is an adequately refined FE mesh, combined with interface elements with tension cut-off between the soil and the structure. The results of the parametric study reveal that the increase of the surcharge load q of the structure leads to larger fault rupture diversion and "smoothing" of the settlement profile, allowing reduction of its stressing. Soil compliance is shown to be beneficial to the stressing of a structure. For a given soil depth H and imposed dislocation h, the rotation $\Delta\theta$ of the structure is shown to be a function of:

I. Anastasopoulos (✉) · G. Gazetas
National Technical University, Athens, Greece
e-mail: ianast@civil.ntua.gr

A. Callerio · E. Faccioli · A. Masella · R. Paolucci
Studio Geotecnico Italiano, Milan, Italy

M. F. Bransby
University of Auckland, Auckland, New Zealand

M. C. R. Davies · A. El Nahas
University of Dundee, Dundee, UK

A. Pecker · E. Rossignol
Geodynamique et Structure, Paris, France

(a) its location relative to the fault rupture; (b) the surcharge load q; and (c) soil compliance.

Keywords Fault rupture propagation · Soil–structure-interaction · Centrifuge model tests · Strip foundation

1 Introduction

Numerous cases of devastating effects of earthquake surface fault rupture on structures were observed in the 1999 earthquakes of Kocaeli, Düzce, and Chi-Chi. However, examples of satisfactory, even spectacular, performance of a variety of structures also emerged (Youd et al. 2000; Erdik 2001; Bray 2001; Ural 2001; Ulusay et al. 2002; Pamuk et al. 2005). In some cases the foundation and structure were quite strong and thus either forced the rupture to deviate or withstood the tectonic movements with some rigid-body rotation and translation but without damage (Anastasopoulos and Gazetas 2007a, b; Faccioli et al. 2008). In other cases structures were quite ductile and deformed without failing. Thus, the idea (Duncan and Lefebvre 1973; Niccum et al. 1976; Youd 1989; Berill 1983) that a structure can be designed to survive with minimal damage a surface fault rupture re-emerged.

The work presented herein was motivated by the need to develop quantitative understanding of the interaction between a rupturing dip-slip (normal or reverse) fault and a variety of foundation types. In the framework of the *QUAKER* research project, an integrated approach was employed, comprising three interrelated steps:

- Field studies (Anastasopoulos and Gazetas 2007a; Faccioli et al. 2008) of documented case histories motivated our investigation and offered material for calibration of the theoretical methods and analyses,
- Carefully controlled geotechnical centrifuge model tests (Bransby et al. 2008a, b) helped in developing an improved understanding of mechanisms and in acquiring a reliable experimental data base for validating the theoretical simulations, and
- Analytical numerical methods calibrated against the above field and experimental data offered additional insight into the nature of the interaction, and were used in developing parametric results and design aids.

This paper summarises the methods and the results of the third step. More specifically:

(i) Three different finite element (FE) analysis methods are presented and calibrated through available soil data.
(ii) The three FE analysis methods are validated against four centrifuge experiments conducted at the University of Dundee, Scotland. Two experiments are used as a benchmark for the "free-field" part of the problem, and two more for the interaction of the outcropping dislocation with rigid strip foundations.
(iii) One of these analysis methods is utilised in conducting a short parametric study on the interaction of typical residential structures with a normal fault rupture.

The problem studied in this paper is portrayed in Fig. 1. It refers to a uniform cohesionless soil deposit of thickness H at the base of which a dip-slip fault, dipping at angle a (measured from the horizontal), produces downward or upward displacement, of vertical component h. The offset (i.e., the differential displacement) is applied to the right part of the model quasi-statically in small consecutive steps.

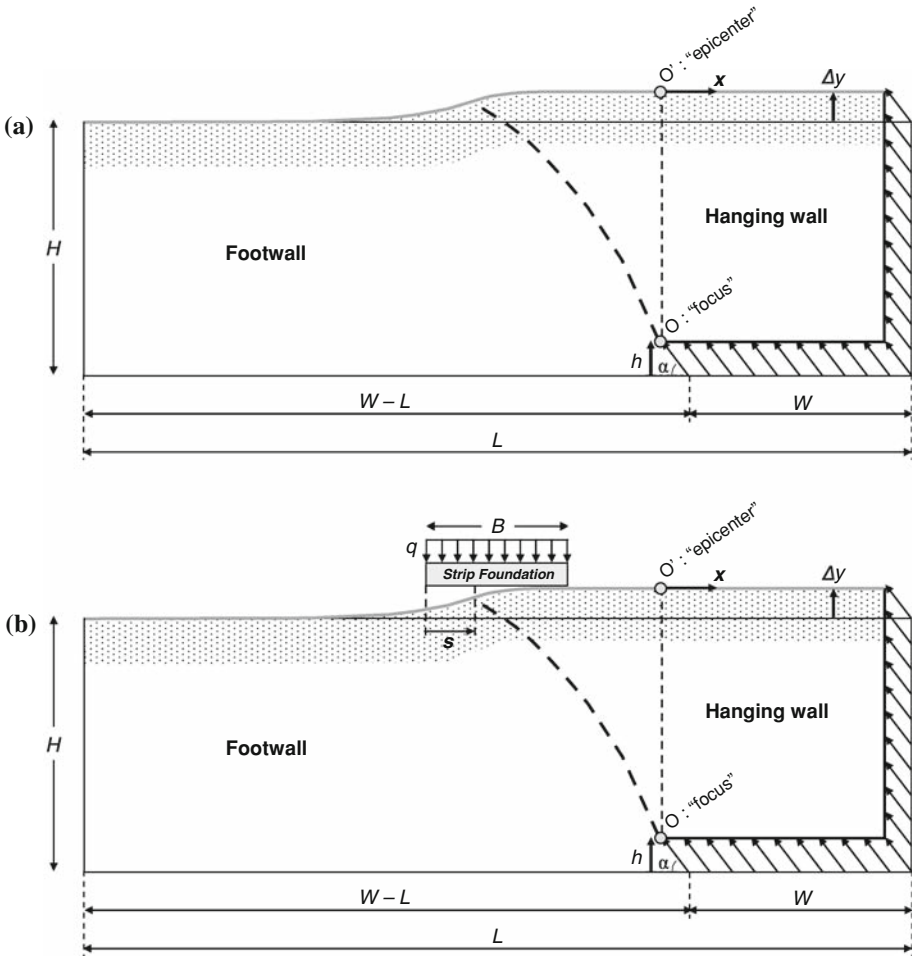

Fig. 1 Definition and geometry of the studied problem: (**a**) Propagation of the fault rupture in the free field, and (**b**) Interaction with strip foundation of width B subjected to uniform load q. The left edge of the foundation is at distance s from the free-field fault outcrop

2 Centrifuge model testing

A series of centrifuge model tests have been conducted in the beam centrifuge of the University of Dundee (Fig. 2a) to investigate fault rupture propagation through sand and its interaction with strip footings (Bransby et al. 2008a, b). The tests modelled soil deposits of depth H ranging from 15 to 25 m. They were conducted at accelerations ranging from 50 to 115 g.

A special apparatus was developed in the University of Dundee to simulate normal and reverse faulting. A central guidance system and three aluminum wedges were installed to impose displacement at the desired dip angle. Two hydraulic actuators were used to push on the side of a split shear box (Fig. 2a) up or down, simulating reverse or normal faulting, respectively. The apparatus was installed in one of the University of Dundee's centrifuge strongboxes (Fig. 2b). The strongbox contains a front and a back transparent Perspex plate, through which the models are monitored in flight. More details on the experimental setup can be found in Bransby et al. (2008a). Displacements (vertical and horizontal) at different

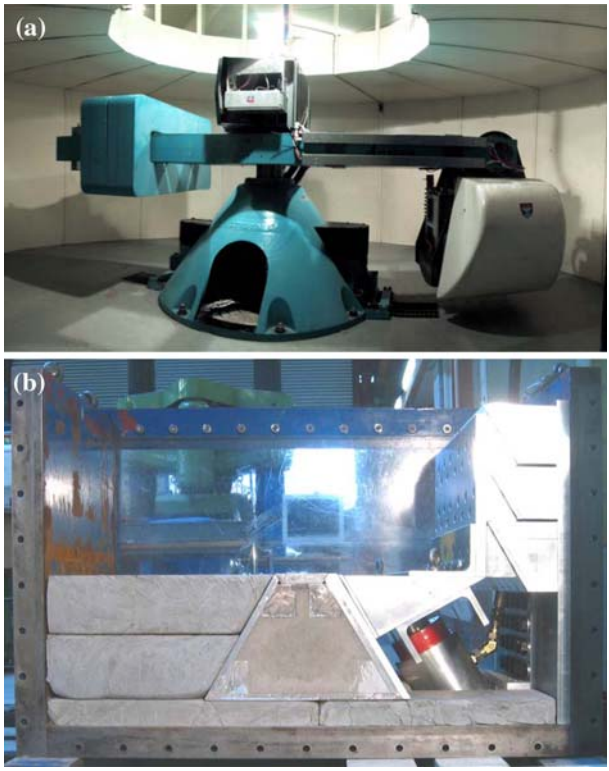

Fig. 2 (**a**) The geotechnical centrifuge of the University of Dundee; (**b**) the apparatus for the experimental simulation of fault rupture propagation through sand

positions within the soil specimen were computed through the analysis of a series of digital images captured as faulting progressed using the Geo-PIV software (White et al. 2003).

Soil specimens were prepared within the split box apparatus by pluviating dry Fontainebleau sand from a specific height with controllable mass flow rate. Dry sand samples were prepared at relative densities of 60%. Fontainebleau sand was used so that previously published laboratory element test data (e.g Gaudin 2002) could be used to select drained soil parameters for the finite element analyses.

The experimental simulation was conducted in two steps. First, fault rupture propagation though soil was modelled in the absence of a structure (Fig. 1a), representing the free-field part of the problem. Then, strip foundations were placed at a pre-specified distance s from the free-field fault outcrop (Fig. 1b), and new tests were conducted to simulate the interaction of the fault rupture with strip foundations.

3 Methods of numerical analysis

Three different numerical analysis approaches were developed, calibrated, and tested. Three different numerical codes were used, in combination with soil constitutive models ranging from simplified to more sophisticated. This way, three methods were developed, each one corresponding to a different level of sophistication:

(a) *Method 1*, using the commercial FE code PLAXIS (2006), in combination with a simple non-associated elastic-perfectly plastic Mohr-Coulomb constitutive model for soil;

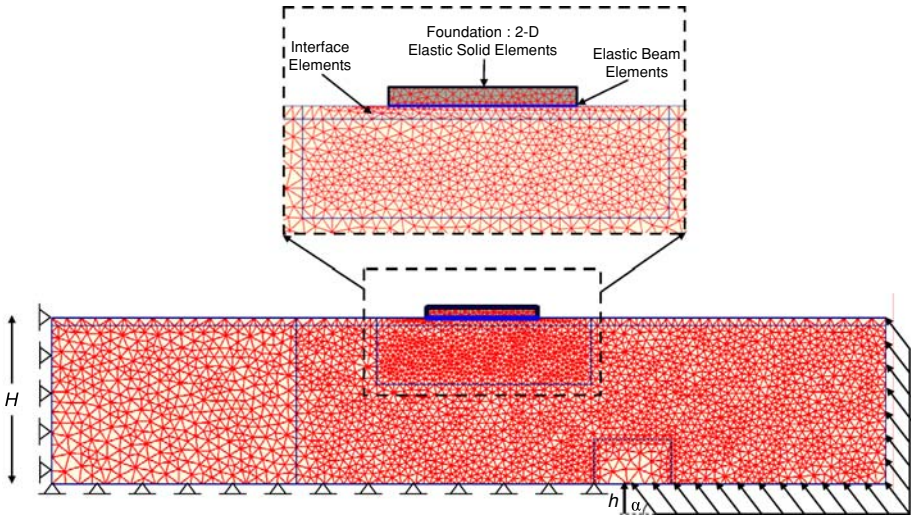

Fig. 3 Method 1 (Plaxis) finite element diecretisation

(b) *Method 2*, utilising the commercial FE code ABAQUS (2004), combined with a modified Mohr-Coulomb constitutive soil model taking account of strain softening; and
(c) *Method 3*, making use of the FE code *DYNAFLOW* (Prevost 1981), along with the sophisticated multi-yield constitutive model of Prevost (1989, 1993).

Centrifuge model tests that were conducted in the University of Dundee were used to validate the effectiveness of the three different numerical methodologies. The main features, the soil constitutive models, and the calibration procedure for each one of the three analysis methodologies are discussed in the following sections.

3.1 Method 1

3.1.1 Finite element modeling approach

The first method uses PLAXIS (2006), a commercial geotechnical FE code, capable of 2D plane strain, plane stress, or axisymmetric analyses. As shown in Fig. 3, the finite element mesh consists of 6-node triangular plane strain elements. The characteristic length of the elements was reduced below the footing and in the region where the fault rapture is expected to propagate. Since a remeshing technique (probably the best approach when dealing with large deformation problems) is not available in *PLAXIS*, at the base of the model and near the fault starting point, larger elements were introduced to avoid numerical inaccuracies and instability caused by ill conditioning of the element geometry during the displacement application (i.e. node overlapping and element distortion).

The foundation system was modeled using a two-layer compound system, consisting of (see Fig. 3):

- The footing itself, discretised by very stiff 2D elements with linear elastic behaviour. The pressure applied by the overlying building structure has been imposed to the models through the self weight of the foundation elements.

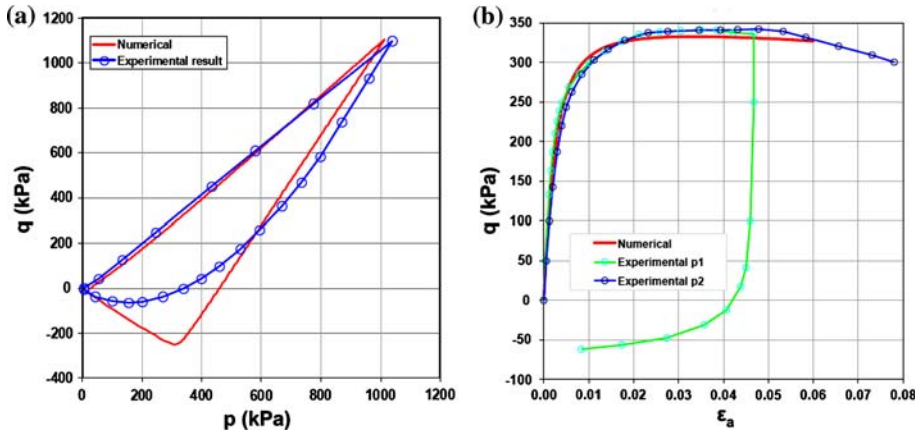

Fig. 4 Method 1: Calibration of constitutive model parameters utilising the FE code Tochnog; (**a**) oedometer test; (**b**) Triaxial test, p = 90 kPa

- Beam elements attached to the nodes at the bottom of the foundation, with stiffness parameters lower than those of the footing to avoid a major stiffness discontinuity between the underlying soil and the foundation structure.
- The beam elements are connected to soil elements through an interface with a purely frictional behaviour and the same friction angle φ with the soil. The interface has a tension cut-off, which causes a gap to develop between soil and foundation in case of detachment.

Due to the large imposed displacement reached during the centrifuge tests (more than 3 m in several cases), with a relative displacement of the order of 10% of the modeled soil height, the large displacement Lagrangian description was adopted.

After an initial phase in which the geostatic stresses were allowed to develop, the fault displacement has been monotonically imposed both on the right side and the right bottom boundaries, while the remaining boundaries of the model have been fixed in the direction perpendicular to the side (Fig. 3), so as to reproduce the centrifuge test boundary conditions.

3.1.2 Soil constitutive model and calibration

The constitutive model adopted for all of the analyses is the standard Mohr-Coulomb formulation implemented in *PLAXIS*. The calibration of the elastic and strength parameters of the soil had been conducted during the earlier phases of the project by means of the FEM code Tochnog (see the developer's home page http://tochnog.sourceforge.net), adopting a rather refined and user-defined constitutive model for sand. This model was calibrated with a set of experimental data available on Fontainebleau sand (Gaudin 2002). Oedometer tests (Fig. 4a) and drained triaxial compression tests (Fig. 4b) have been simulated, and sand model parameters were calibrated to reproduce the experimental results. The user-defined model implemented in Tochnog included a yielding function at the critical state, which corresponds to the Mohr-Coulomb failure criterion. A subset of those parameters was then utilised in the analysis conducted using the simpler Mohr-Coulomb model of *PLAXIS*:

- Angle of friction $\varphi = 37\,^\circ$
- Young's Modulus $E = 675$ MPa
- Poisson's ratio $\nu = 0.35$
- Angle of Dilation $\psi = 0\,^\circ$

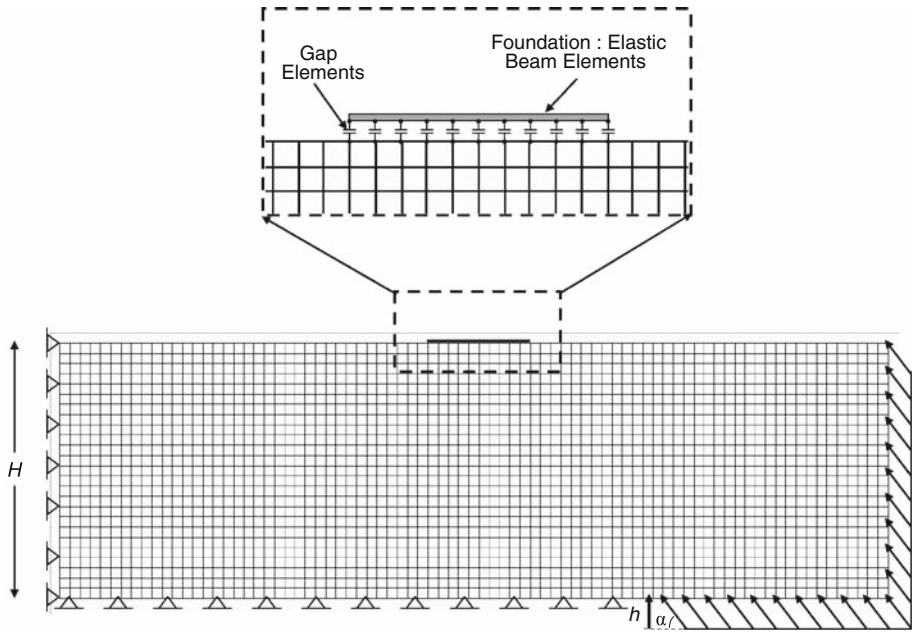

Fig. 5 Method 2 (Abaqus) finite element diecretisation

The assumption of $\psi = 0$ and $\nu = 0.35$, although not intuitively reasonable, was proven to provide the best fit to experimental data, both for normal and reverse faulting.

3.2 Method 2

3.2.1 Finite element modeling approach

The FE mesh used for the analyses is depicted in Fig. 5 (for the reverse fault case). The soil is now modelled with quadrilateral plane strain elements of width $d_{FE} = 1$ m. The foundation, of width B, is modelled with beam elements. It is placed on top of the soil model and connected through special contact (gap) elements. Such elements are infinitely stiff in compression, but offer no resistance in tension. In shear, their behaviour follows Coulomb's friction law.

3.2.2 Soil constitutive model

Earlier studies have shown that soil behaviour after failure plays a major role in problems related to shear-band formation (Bray 1990; Bray et al. 1994a, b). Relatively simple elastoplastic constitutive models, with Mohr-Coulomb failure criterion, in combination with strain softening have been shown to be effective in the simulation of fault rupture propagation through soil (Roth et al. 1981, 1982; Loukidis 1999; Erickson et al. 2001), as well as for modelling the failure of embankments and slopes (Potts et al. 1990, 1997).

In this study, we apply a similar elastoplastic constitutive model with Mohr-Coulomb failure criterion and isotropic strain softening (Anastasopoulos 2005). Softening is introduced by reducing the mobilised friction angle φ_{mob} and the mobilised dilation angle ψ_{mob} with the increase of plastic octahedral shear strain:

$$\varphi_{mob} = \left\{ \begin{array}{ll} \varphi_p - \frac{\varphi_p - \varphi_{res}}{\gamma_f^P} \gamma_{oct}^P, & \text{for } 0 \le \gamma_{oct}^P < \gamma_f^P \\ \varphi_{res}, & \text{for } \gamma_{oct}^P \ge \gamma_f^P \end{array} \right\} \tag{1}$$

$$\psi_{mob} = \left\{ \begin{array}{ll} \psi_p \left(1 - \frac{\gamma_{oct}^P}{\gamma_f^P} \right), & \text{for } 0 \le \gamma_{oct}^P < \gamma_f^P \\ \psi_{res}, & \text{for } \gamma_{oct}^P \ge \gamma_f^P \end{array} \right\} \tag{2}$$

where φ_p and φ_{res} the ultimate mobilised friction angle and its residual value; ψ_p the ultimate dilation angle; γ_f^P the plastic octahedral shear strain at the end of softening.

3.2.3 Constitutive model calibration

Constitutive model parameters are calibrated through the results of direct shear tests. Soil response can be divided in four characteristic phases (Anastasopoulos et al. 2007):

(a) *Quasi-elastic behavior*: The soil deforms quasi-elastically (Jewell and Roth 1987), up to a horizontal displacement δx_y.
(b) *Plastic behavior*: The soil enters the plastic region and dilates, reaching peak conditions at horizontal displacement δx_p.
(c) *Softening behavior*: Right after the peak, a single horizontal shear band develops (Jewell and Roth 1987; Gerolymos et al. 2007).
(d) *Residual behavior*: Softening is completed at horizontal displacement δx_f ($\delta y / \delta x \approx 0$). Then, deformation is accumulated along the developed shear band.

Quasi-elastic behaviour is modelled as linear elastic, with secant modulus G_S linearly increasing with depth:

$$G_S = \frac{\tau_y}{\gamma_y} \tag{3}$$

where τ_y and γ_y: the shear stress and strain at first yield, directly measured from test data.

After peak conditions are reached, it is assumed that plastic shear deformation takes place within the shear band, while the rest of the specimen remains elastic (Shibuya et al. 1997). Scale effects have been shown to play a major role in shear localisation problems (Stone and Muir Wood 1992; Muir Wood and Stone 1994; Muir Wood 2002). Given the unavoidable shortcomings of the FE method, an approximate simplified scaling method (Anastasopoulos et al. 2007) is employed.

The constitutive model was encoded in the FE code ABAQUS (2004). Its capability to reproduce soil behaviour has been validated through a series of FE simulations of the direct shear test (Anastasopoulos 2005). Figure 6 depicts the results of such a simulation of dense Fontainebleau sand ($D_r \approx 80\%$), and its comparison with experimental data by Gaudin (2002). Despite its simplicity and (perhaps) lack of generality, the employed constitutive model captures the predominant mode of deformation of the problem studied herein, providing a reasonable simplification of complex soil behaviour.

3.3 Method 3

3.3.1 Finite element modeling approach

The finite element model used for the analyses is shown for the normal fault case in Fig. 7. The soil is modeled with square, quadrilateral, plane strain elements, of width $d_{FE} = 0.5\,\text{m}$.

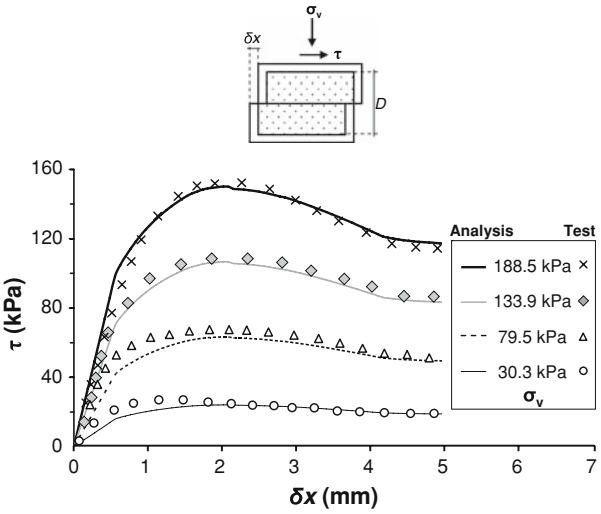

Fig. 6 Method 2: Calibration of constitutive model—comparison between laboratory direct shear tests on Fontainebleau sand (Gaudin 2002) and the results of the constitutive model

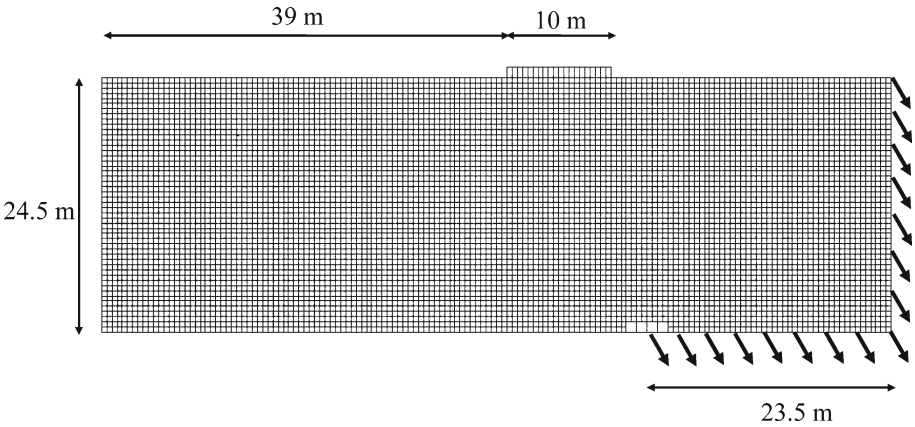

Fig. 7 Method 3 (Dynaflow) finite element diecretisation

Each element is defined with four nodes with two degrees of freedom at each node. The foundation, of width B, is modeled with quadrilateral infinitely stiff elements. It is connected to the soil model with contact elements. The latter are used to impose inequality constraints between the soil and the foundation; they are defined with three nodes and a penalty parameter. When the soil is in contact with the foundation, perfect friction is imposed; when separation between the foundation and the soil occurs no forces are transmitted from the soil to the foundation.

The numerical problem is solved with an implicit explicit predictor (multi) corrector scheme; the non linear implicit solution algorithm used is a quasi Newton BFGS algorithm with line search (Strang strategy) at each time step and a large displacement option. The incremental displacement at the fault location is equal to 1 cm.

3.3.2 Soil constitutive Model

The constitutive model is the multi-yield constitutive model developed by Prevost (1989, 1993). It is a kinematic hardening model, based on a relatively simple plasticity theory (Prevost 1985) and is applicable to both cohesive and cohesionless soils. The concept of a "field of work-hardening moduli" (Iwan 1967; Mróz 1967; Prevost 1977), is used by defining a collection f_0, $f_1, \ldots, f_n$ of nested yield surfaces in the stress space. Von Mises type surfaces are employed for cohesive materials, and Drucker-Prager/Mohr-Coulomb type surfaces are employed for frictional materials (sands).

The *yield surfaces* define regions of constant shear moduli in the stress space, and in this manner the model discretises the smooth elastic-plastic stress–strain curve into n linear segments. The outermost surface f_n represents a failure surface. In addition, accounting for experimental evidence from tests on frictional materials (e.g. Lade 1987), a non-associative *plastic flow rule* is used for the dilatational component of the plastic potential.

Finally, the material hysteretic behavior and shear stress-induced anisotropic effects are simulated by a *kinematic rule*. Upon contact, the yield surfaces are translated in the stress space by the stress point, and the direction of translation is selected such that the yield surfaces do not overlap, but remain tangent to each other at the stress point.

3.3.3 Constitutive model parameters

The required constitutive parameters of the multi-yield constitutive soil model are summarised as follows (Popescu and Prevost 1995):

a. *Initial state parameters*: mass density of the solid phase ρ_s, and for the case of porous saturated media, porosity n^w and permeability k.
b. *Low strain elastic parameters*: low strain moduli G_0 and B_0. The dependence of the moduli on the mean effective normal stress p', is assumed to be of the following form:

$$G = G_0 \left(\frac{p'}{p'_0}\right)^n \quad B = B_0 \left(\frac{p'}{p'_0}\right)^n \tag{4}$$

and is accounted for, by introducing two more parameters: the power exponent n and the reference effective mean normal stress p'_0.
c. *Yield and failure parameters*: these parameters describe the position a_i, size M_i and plastic modulus H'_i, corresponding to each yield surface f_i, $i = 0, 1, \ldots n$. For the case of pressure sensitive materials, a modified hyperbolic expression proposed by Prevost (1989) and Griffiths and Prévost (1990) is used to simulate soil stress–strain relations. The necessary parameters are: (i) the initial gradient, given by the small strain shear modulus G_0, and (ii) the stress (function of the friction angle at failure φ and the stress path) and strain, $\varepsilon_{dev}^{\max}$, levels at failure. Hayashi et al. (1992) improved the modified hyperbolic model by introducing a new parameter—a—depending on the maximum grain size $D_{\max}$ and uniformity coefficient C_u. Finally, the coefficient of lateral stress K_0 is necessary to evaluate the initial positions a_i of the yield surfaces.
d. *Dilation parameters*: these are used to evaluate the volumetric part of the plastic potential and consist of: (i) the *dilation* (or phase transformation) angle $\bar{\varphi}$, and (ii) the *dilation parameter* X_{pp}, which is the scale parameter for the plastic dilation, and depends basically on relative density and sand type (fabric, grain size).

With the exception of the dilation parameter, all the required constitutive model parameters are traditional soil properties, and can be derived from the results of conventional laboratory

Table 1 Constitutive model parameters used in method 3

Number of yield surfaces	20	Power exponent n	0.5
Shear modulus G at stress p_1 (kPa)	75,000	Bulk modulus at stress p_1 (kPa)	200,000
Unit mass ρ (t.m^{-3})	1.63	Cohesion	0
Reference mean normal stress p_1 (kPa)	100	Lateral stress coefficient (K_0)	0.5
Dilation angle in compression (°)	31	Dilation angle in extension (°)	31
Ultimate friction angle in compression (°)	41.8	Ultimate friction angle in extension (°)	41.8
Dilation parameter X_{pp}	1.65		
Max shear strain in compression	0.08	Max shear strain in extension	0.08
Generation coefficient in compression α_c	0.098	Generation coefficient in extension α_e	0.095
Generation coefficient in compression α_{lc}	0.66	Generation coefficient in extension α_{le}	0.66
Generation coefficient in compression α_{uc}	1.16	Generation coefficient in extension α_{ue}	1.16

(e.g. triaxial, simple shear) and in situ (e.g. cone penetration, standard penetration, wave velocity) soil tests. The dilational parameter can be evaluated on the basis of results of liquefaction strength analysis, when available; further details can be found in Popescu and Prevost (1995) and Popescu (1995).

Since in the present study the sand material is dry, the cohesionless material was modeled as a one-phase material. Therefore neither the soil porosity, n^w, nor the permeability, k, are needed.

For the *shear stress–strain curve generation*, given the maximum shear modulus G_1, the maximum shear stress $\tau_{\max}$ and the maximum shear strain $\gamma_{\max}$, the following functional relationship has been chosen:

For $y = \tau/\tau_{\max}$ and $x = \gamma/\gamma_r$, with $\gamma_r = \tau_{\max}/G_1$, then:

$$y = \exp(-ax)\, f(x, x_l) + (1 - \exp(-ax))\, f(x, x_u) \tag{5}$$

where:

$$f(x, x_i) = \left[(2x/x_i + 1)^{x_i} - 1\right] / \left[(2x/x_i + 1)^{x_i} + 1\right]$$

where a, x_l and x_u are material parameters. For further details, the reader is referred to Hayashi et al. (1992).

The constitutive model is implemented in the computer code *DYNAFLOW* (Prevost 1981) that has been used for the numerical analyses.

3.3.4 Calibration of model constitutive parameters

To calibrate the values of the constitutive parameters, numerical triaxial tests were simulated with *DYNAFLOW* at three different confining pressures (30, 60, 90 kPa) and compared with the results of available physical tests conducted on the same material at the same confining pressures. The parameters are defined based on the shear stress versus axial strain curve and volumetric strain versus axial strain curve. Figure 8 illustrates the comparisons between numerical simulations and physical tests in terms of volumetric strain and shear stress versus

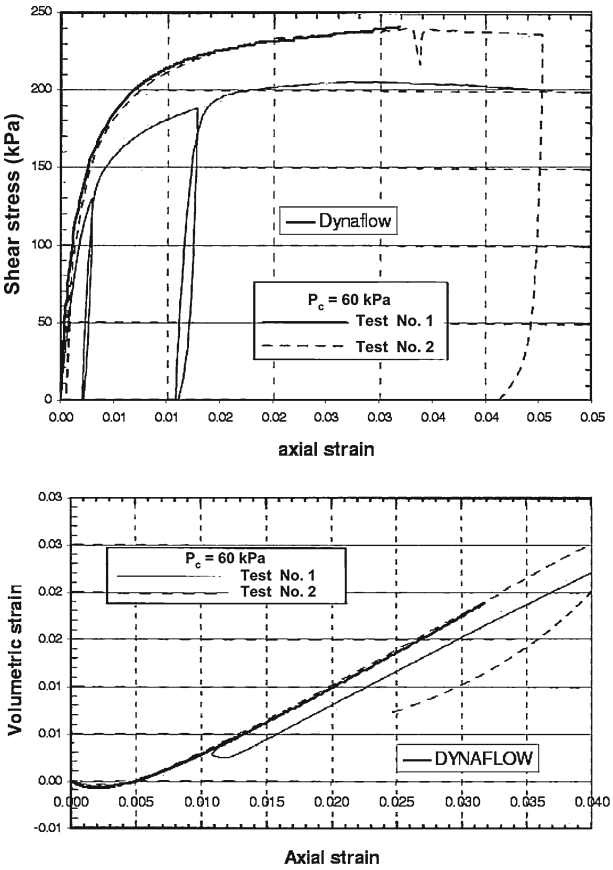

Fig. 8 Method 3: Calibration of constitutive model parameters; triaxial tests at 60 kPa

axial strain for the test conducted with a confining pressure of 60 kPa. The parameters finally retained for a complete definition of the constitutive model used for the numerical finite element analyses are listed in Table 1.

4 Comparison between numerical analysis approaches

To evaluate the effectiveness of the developed numerical analysis approaches, we compare experimental data of centrifuge model tests with analytical predictions. First, the comparison is conducted for the free-field part of the problem, to highlight the capability of the different models in predicting the rupture path, the location of fault outcropping (defined as the point where the steepest gradient is observed), and the deformation of the ground surface. Two centrifuge tests are utilised for this purpose: (a) Test 12, normal faulting at 60°; and (b) Test 28, reverse faulting at 60°. Since the free-field cases had not been analysed with the more elaborate Method 3, the comparison is restricted to the first two methods (1 and 2).

Then, two other centrifuge tests with shallow foundations are compared to shed more light in the robustness of the FE approaches with respect to Fault Rupture–Soil–Foundation–

Table 2 Summary of main attributes of the centrifuge model tests

Test	Faulting	B (m)	q (kPa)	s (m)	g-Level[a]	D_r (%)	H (m)	L (m)	W (m)	h_{max} (m)
12	Normal	Free—field			115	60.2	24.7	75.7	23.5	3.15
28	Reverse	Free—field			115	60.8	15.1	75.7	23.5	2.59
14	Normal	10	91	2.9	115	62.5	24.6	75.7	23.5	2.49
29	Reverse	10	91	9.2	115	64.1	15.1	75.7	23.5	3.30

[a] Centrifugal acceleration

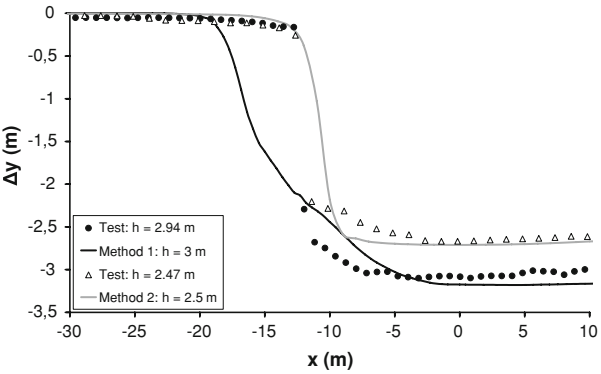

Fig. 9 Test 12—Free-field fault rupture propagation through $D_r = 60\%$ Fontainebleau sand ($\alpha = 60°$): Comparison of numerical with experimental vertical displacement of the surface for bedrock dislocation $h = 3.0$ m (Method 1) and 2.5 m (Method 2) [all displacements are given in prototype scale]

Structure Interaction (FR-SFSI): (i) Test 14, normal faulting at 60°; and (ii) Test 29, reverse faulting at 60°. In this case, the comparison is conducted for all of the developed numerical analysis approaches.

The main attributes of the four centrifuge model tests used for the comparisons are synopsised in Table 2, while more details can be found in Bransby et al. (2008a, b).

4.1 Free-field fault rupture propagation

4.1.1 Test12—normal 60°

This test was conducted at 115 g on medium-loose ($D_r = 60\%$) Fontainebleau sand, simulating normal fault rupture propagation through an $H = 25$ m soil deposit. The comparison between analytical predictions and experimental data is depicted in Fig. 9 in terms of vertical displacement Δy at the ground surface. All displacements are given in prototype scale. While the analytical prediction of Method 1 is compared with test data for $h = 3.0$ m, in the case of Method 2 the comparison is conducted at slightly lower imposed bedrock displacement: $h = 2.5$ m. This is due to the fact that the numerical analysis with Method 2 was conducted without knowing the test results, and at that time it had been agreed to set the maximum displacement equal to $h_{max} = 2.5$ m. However, when test results were publicised, the actually attained maximum displacement was larger, something that was taken into account in the analyses with Method 1.

As illustrated in Fig. 9, Method 2 predicts almost correctly the location of fault outcropping, at about—10 m from the "epicenter", with discrepancies limited to 1 or 2 m. The deformation can be seen to be slightly more localised in the centrifuge test, but the comparison between analytical and experimental shear zone thickness is quite satisfactory. The vertical displacement profile predicted by Method 1 is also qualitatively acceptable. However, the

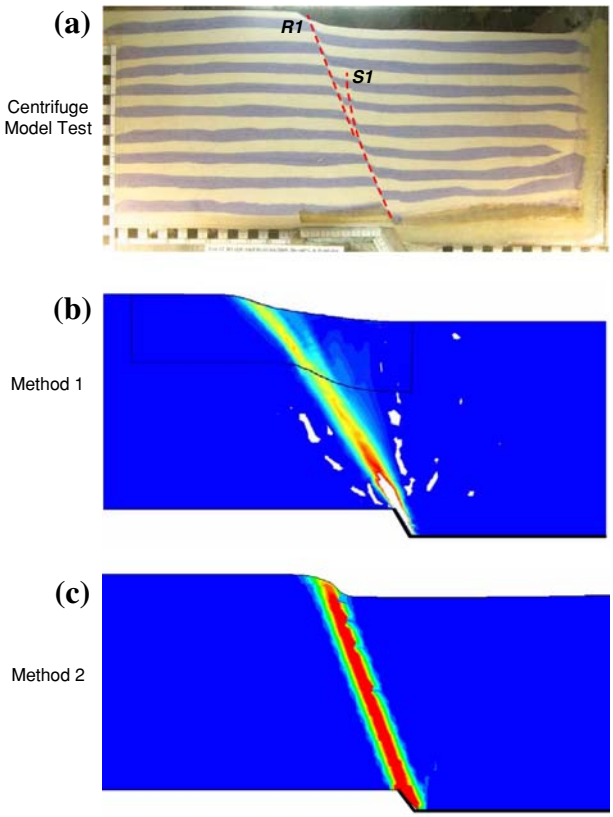

Fig. 10 Test 12—-Normal free-field fault rupture propagation through $H = 25\,\text{m}$ $D_r = 60\%$ Fontainebleau sand: Comparison of (**a**) Centrifuge model test image, compared to FE deformed mesh with shear strain contours of Method 1 (**b**), and Method 2 (**c**), for $h = 2.5\,\text{m}$

location of fault rupture emergence is a few meters to the left compared with the experimental: at about 15 m from the "epicenter" (instead of about 10 m). In addition, the deformation predicted by Method 1 at the ground surface computed using method 1 is widespread, instead of localised at a narrow band.

FE deformed meshes with superimposed shear strain contours are compared with an image from the experiment in Fig. 10, for $h = 2.5\,\text{m}$. In the case of Method 2, the comparison can be seen to be quite satisfactory. However, it is noted that the secondary rupture ($S1$) that forms in the experiment to the right of the main shear plane ($R1$) is not predicted by Method 2. Also, experimental shear strain contours (not shown herein) are a little more diffuse than the FE prediction. Overall, the comparison is quite satisfactory.

In the case of Method 1, the quantitative details are not in satisfactory agreement, but the calculation reveals a secondary rupture to the right of the main shear zone, consistent with the experimental image.

4.1.2 Test 28—reverse 60°

This test was also conducted at 115 g and the sand was of practically the same relative density ($D_r = 61\%$). Given that reverse fault ruptures require larger normalised bedrock

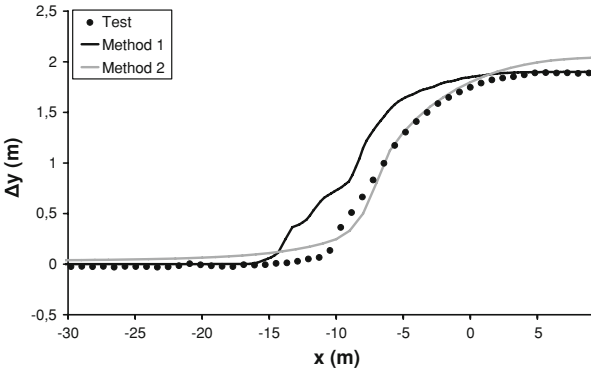

Fig. 11 Test 28—Reverse free-field fault rupture propagation through $H = 15\,\text{m}$ $D_r = 60\%$ Fontainebleau sand: Comparison of numerical with experimental vertical displacement of the surface for bedrock dislocation $h = 2.0\,\text{m}$ (all displacements are given in prototype scale)

displacement h/H to propagate all the way to the surface (e.g. Cole and Lade 1984; Lade et al. 1984; Anastasopoulos et al. 2007; Bransby et al. 2008b), the soil depth was set at $H = 15\,\text{m}$. This way, a larger h/H could be achieved with the same actuator.

Figure 11 compares the vertical displacement Δy at the ground surface predicted by the numerical analysis to experimental data, for $h = 2.0\,\text{m}$. This time, both models predict correctly the location of fault outcropping (defined as the point where the steepest gradient is observed). In particular, Method 1 achieves a slightly better prediction of the outcropping location: $-10\,\text{m}$ from the epicentre (i.e., a difference of 1 m only, to the other direction). Method 2 predicts the fault outbreak at about $-7\,\text{m}$ from the "epicenter", as opposed to about $-9\,\text{m}$ of the centrifuge model test (i.e., a discrepancy of about 2 m).

Figure 12 compares FE deformed meshes with superimposed shear strain contours with an image from the experiment, for $h = 2.5\,\text{m}$. In the case of Method 2, the numerical analysis seems to predict a distinct fault scarp, with most of the deformation localised within it. In contrast, the localisation in the experiment is clearly more intense, but the fault scarp at the surface is much less pronounced: the deformation is widespread over a larger area. The analysis with Method 1 is successful in terms of the outcropping location. However, instead of a single rupture, it predicts the development of two main ruptures ($R1$ and $R2$), accompanied by a third shear plane in between. Although such soil response has also been demonstrated by other researchers (e.g. Loukidis and Bouckovalas 2001), in this case the predicted multiple rupture planes are not consistent with experimental results.

4.2 Interaction with strip footings

Having validated the effectiveness of the developed numerical analysis methodologies in simulating fault rupture propagation in the free-field, we proceed to the comparisons of experiments with strip foundations: one for normal (Test 14), and one for reverse (Test 29) faulting. This time, the comparison is extended to all three methods.

4.2.1 Test 14—normal 60°

This test is practically the same with the free-field Test 12, with the only difference being the presence of a $B = 10\,\text{m}$ strip foundation subjected to a bearing pressure $q = 90\,\text{kPa}$. The foundation is positioned so that the free-field fault rupture would emerge at distance $s = 2.9\,\text{m}$ from the left edge of the foundation.

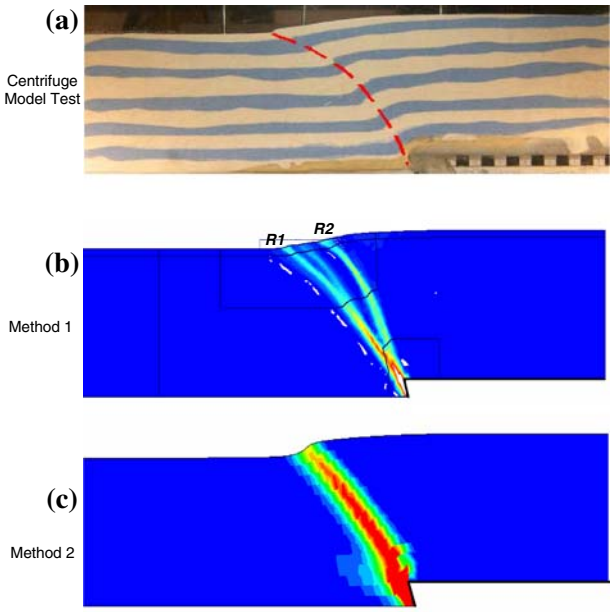

Fig. 12 Test 28—Reverse free-field fault rupture propagation through $H = 15\,\text{m}$ $D_r = 60\%$ Fontainebleau sand: Comparison of (**a**) Centrifuge model test image, compared to FE deformed mesh with shear strain contours of Method 1 (**b**), and Method 2 (**c**), for $h = 2.5\,\text{m}$

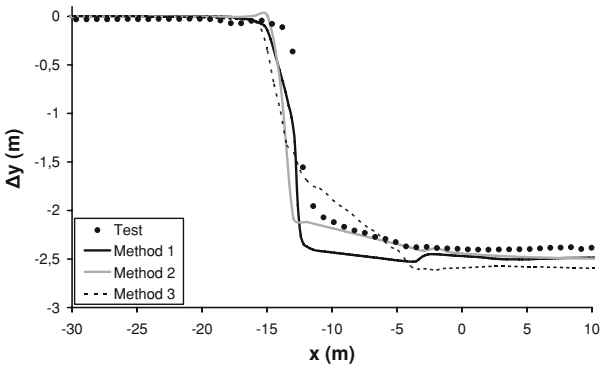

Fig. 13 Test 14—Interaction of normal $\alpha = 60^\circ$ fault rupture, through $H = 25\,\text{m}$ sand deposit, with rigid $B = 10\,\text{m}$ foundation subjected to surcharge load $q = 90\,\text{kPa}$, positioned at distance $s = 2.9\,\text{m}$: Vertical displacement profile at the surface, $h = 2.5\,\text{m}$ (all displacements are given in prototype scale)

Figure 13 compares experimental results with numerical predictions in terms of vertical displacement Δy at the ground surface for bedrock displacement $h = 2.5\,\text{m}$. The agreement is satisfactory for all three modelling methodologies. All FE analyses predict correctly the diversion of the fault rupture to the left of the foundation. While in Test 12 (free-field) the rupture outcropped at $d = -10\,\text{m}$ from the "epicenter", in the presence of the foundation it is diverted to emerge at $d = -13\,\text{m}$. Despite this diversion, the foundation is subjected to rigid body rotation $\Delta\theta$.

Figure 14 shows that the three numerical methodologies yield different results in terms of foundation rotation $\Delta\theta$ with respect to h. The numerical prediction obtained with Method 1 leads to an underestimation of $\Delta\theta$ (probably due to the $\psi = 0^\circ$ assumption): for $h = 2.5\,\text{m}$ Method 1 predicts $\Delta\theta = 0.5^\circ$ (instead of 2.1° measured in the experiment). In contrast,

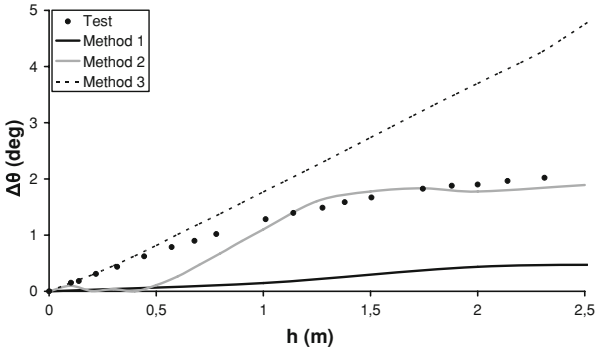

Fig. 14 Test 14—Interaction of normal $\alpha = 60°$ fault rupture, through $H = 25$ m sand deposit, with rigid $B = 10$ m foundation subjected to surcharge load $q = 90$ kPa, positioned at distance $s = 2.9$ m: Foundation rotation $\Delta\theta$ versus bedrock fault offset h

with the exception of the region of small imposed displacement ($h < 1$ m), the prediction of Method 2 is in good agreement with the experiment: at $h = 2.5$ m, the analysis predicts $\Delta\theta = 1.9°$ (compared with 2.1° in the test). Finally, the prediction of Method 3 indicates an almost linear increase of $\Delta\theta$ with imposed bedrock displacement h, leading to overestimation of the footing rotation at large h (probably due to the fact that the model does not take account of strain softening). More specifically, for $h = 2.5$ m, Method 3 predicts $\Delta\theta = 4.8°$ instead of the measured 2.1°, but gives good predictions at small fault offsets ($h \leq 0.5$ m).

A centrifuge model test image is compared with FE computed deformed meshes with superimposed vertical displacement contours in Fig. 15 for $h = 2.5$ m. All three numerical approaches predict correctly the diversion of the main fault rupture ($R1$') to the left of the foundation (towards the footwall). As already discussed, the main difference lies in the foundation rotation $\Delta\theta$. In the experiment, a secondary steep rupture zone, $S1$' (practically the same as $S1$ of Test 12), develops and propagates half the way to the surface before $R1$' is formed (see also Bransby et al. 2008a).

4.2.2 Test 29—reverse 60°

Test 29 is practically the same as free-field Test 28, with the only difference being the presence of a $B = 10$ m strip foundation subjected to $q = 90$ kPa, positioned at $s = 9.2$ m.

Figure 16 compares experimental data with analytical predictions in terms of Δy at the soil surface for $h = 2.5$ m. This time, the differences between the three numerical approaches are negligible, with all three vertical displacement profiles exhibiting similar behaviour, and in general agreement with the experimental observations. All three numerical approaches indicate some soil heave on the left side of the foundation, which may be caused by the compression induced by foundation rotation. However, in the case of Methods 1 and 2, the heave is limited to a smaller area very close to the foundation edge. This behaviour is attributable to the inherent differences of the adopted constitutive models. All three FE models predict correctly the diversion of the rupture path to the right of the foundation, while the differences in terms of foundation rotation $\Delta\theta$ are much smaller than for the normal fault case.

As illustrated in Fig. 17, the numerical prediction of Method 1 generally overestimates $\Delta\theta$: for $h = 2.5$ m Method 1 predicts $\Delta\theta = 2.4°$. The results of Method 2 are different, exhibiting a softening-like behaviour. As a result, $\Delta\theta$ is initially ($h \leq 2$ m) overestimated, but in the end ($h = 2.5$ m) the analysis yields slightly lower $\Delta\theta$ compared to the experiment: 1.4° instead of the measured 1.6°. Method 3 indicates an increase of $\Delta\theta$ with respect to h with an increasing rate. Thus, while at the beginning it underestimates the rotation of the foundation,

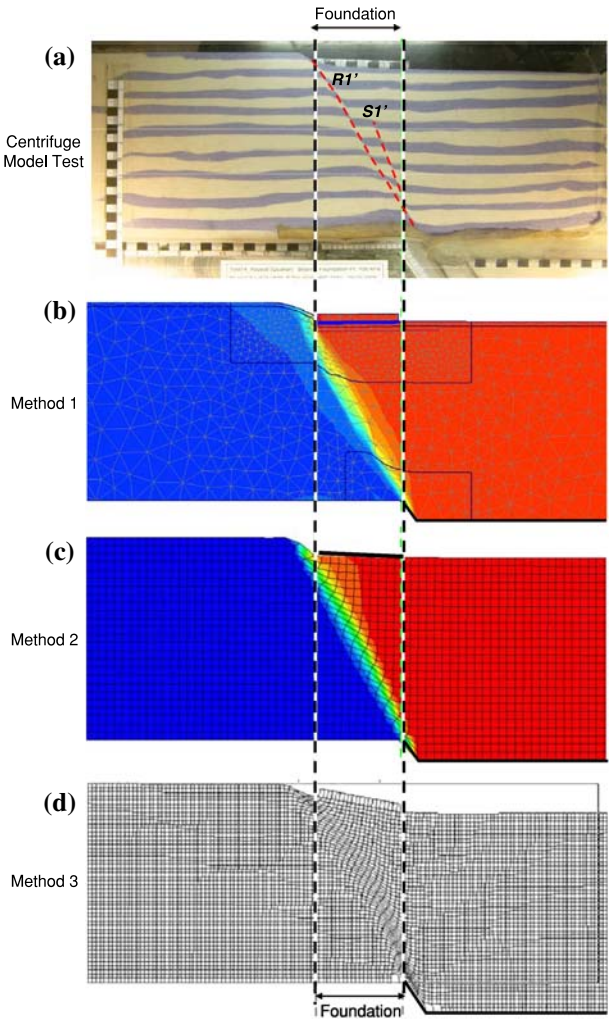

Fig. 15 Test 14—Interaction of normal $\alpha = 60^\circ$ fault rupture, through $H = 25\,\text{m}$ sand deposit, with rigid $B = 10\,\text{m}$ foundation subjected to surcharge load $q = 90\,\text{kPa}$, positioned at distance $s = 2.9\,\text{m}$: Centrifuge model test image (**a**), compared to FE deformed mesh with shear strain contours of Method 1 (**b**), Method 2 (**c**), and Method 3 (**d**), for $h = 2.5\,\text{m}$

at larger imposed displacement h it tends to slightly overestimate it: for $h = 2.5\,\text{m}$, it predicts $\Delta\theta = 2.0^\circ$ instead of the measured 1.6°.

Figure 18 compares a centrifuge model test image with the computed deformed FE meshes with superimposed vertical displacement contours (for $h = 2.5\,\text{m}$). The shear planes predicted by Methods 1 and 2 are quite localised, with plastic deformation within a narrow band, in good agreement with the centrifuge model test. The Method 3-predicted deformed mesh is characterised by a wider shear zone. The Method 1 numerical result can be seen to be in good agreement with the centrifuge test in terms of the soil overlapping at the right edge of the footing. However, in the centrifuge test a secondary localisation is also formed. It initiates from the top-right (footwall-side) edge of the foundation and propagates downwards. This

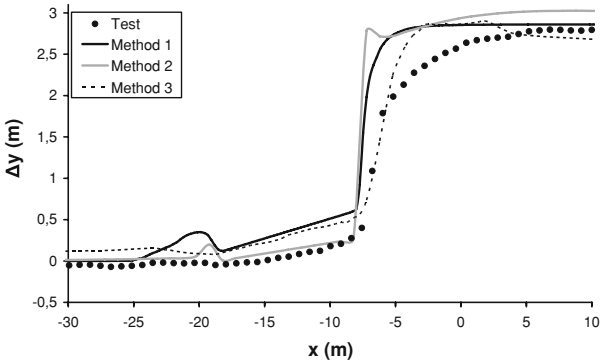

Fig. 16 Test 29—Interaction of reverse $\alpha = 60°$ fault rupture, through $H = 15\,\text{m}$ sand deposit, with rigid $B = 10\,\text{m}$ foundation subjected to surcharge load $q = 90\,\text{kPa}$, positioned at distance $s = 9.2\,\text{m}$: Vertical displacement profile at the surface, $h = 2.5\,\text{m}$ (all displacements are given in prototype scale)

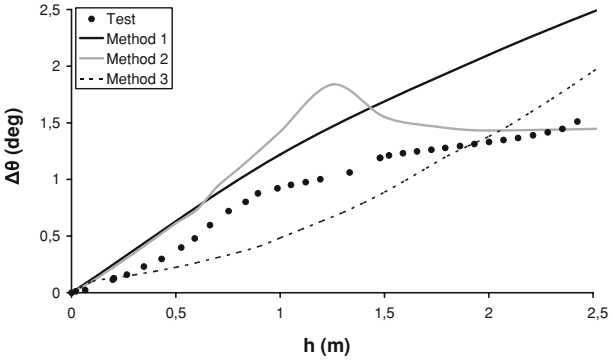

Fig. 17 Test 29—Interaction of reverse $\alpha = 60°$ fault rupture, through $H = 15\,\text{m}$ sand deposit, with rigid $B = 10\,\text{m}$ foundation subjected to surcharge load $q = 90\,\text{kPa}$, positioned at distance $s = 9.2\,\text{m}$: Foundation rotation $\Delta\theta$ versus bedrock fault offset h

takes place at the later stages of the experiment, when the top side of the foundation gains contact with the upwards displacing soil. The numerical analyses cannot possibly capture this feature, since no contact elements have been placed between the side edges of the foundation and the soil surface.

5 Parametric analysis

5.1 Methodology

Having validated the three FE analysis methodologies developed within the *QUAKER* research project, we apply Method 2 to conduct a short parametric study of typical residential structures subjected to normal fault dislocation.

The main factors influencing FR-SFSI are (Anastasopoulos and Gazetas 2007b):

(a) The type and continuity of the foundation system (isolated footings, raft, piles).
(b) The flexural and axial rigidity of the foundation system (e.g. thickness of mat foundation).
(c) The surcharge load of the superstructure.
(d) The stiffness of the superstructure (cross section of structural members, grid spacing).
(e) The soil stiffness and strength.
(f) The position of the structure relative to the fault rupture (distance s).

All of the above factors are examined herein, with the exception of the type of foundation system: given that the continuity of the foundation system has already been shown to be

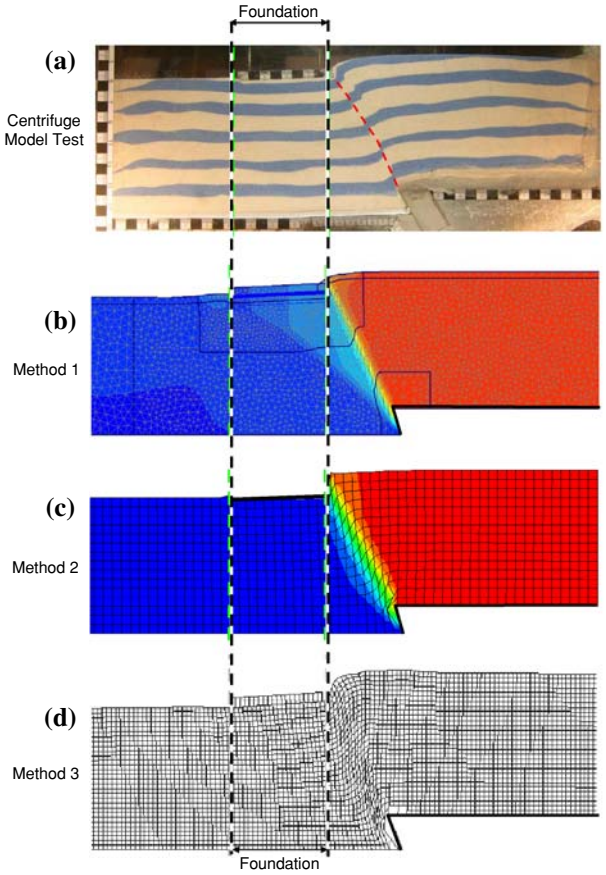

Fig. 18 Test 29—Interaction of reverse $\alpha = 60^\circ$ fault rupture, through $H = 15$ m sand deposit, with rigid $B = 10$ m foundation subjected to surcharge load $q = 90$ kPa, positioned at distance $s = 9.2$ m: Centrifuge model test image (**a**), compared to FE deformed mesh with shear strain contours of Method 1 (**b**), Method 2 (**c**), and Method 3 (**d**), for $h = 2.5$ m

crucial for the response of a structure (Anastasopoulos and Gazetas 2007b; Faccioli et al. 2008), we will focus on buildings resting on mat foundations (slab or box-type).

Without underestimating the general importance of the details of a superstructure, we treat all of the analysed structures as "equivalent" in this respect, changing only the number of storeys. This way it is easier to develop insights on the influence of the type and stiffness of their foundation, and on the effect of the surcharge load on FR-SFSI. Therefore, a typical column grid of 5×5 m is utilised, in combination with a structure width $B = 20$ m. Columns and beams are of 50 cm square cross-section, taking into account the contribution of walls and slabs. Such a hypothesis can be considered as realistic for 2- to 5-story buildings (Anastasopoulos and Gazetas 2007b).

To explore the role of foundation stiffness EI, the equivalent thickness of the slab foundation is varied from $t = 0.2$ to 0.5 m, and 1.3 m, yielding $EI = 2.0 \times 10^5$, 3.1×10^6, and 5.5×10^7 kNm^2. It is noted that the stiffness of the foundation is coupled to its dead load, which is added to the overall equivalent surcharge load of the superstructure, q. The distance of the outcropping fault to the left edge of the structure is also varied: $s = 4$, 10 m, and 16 m

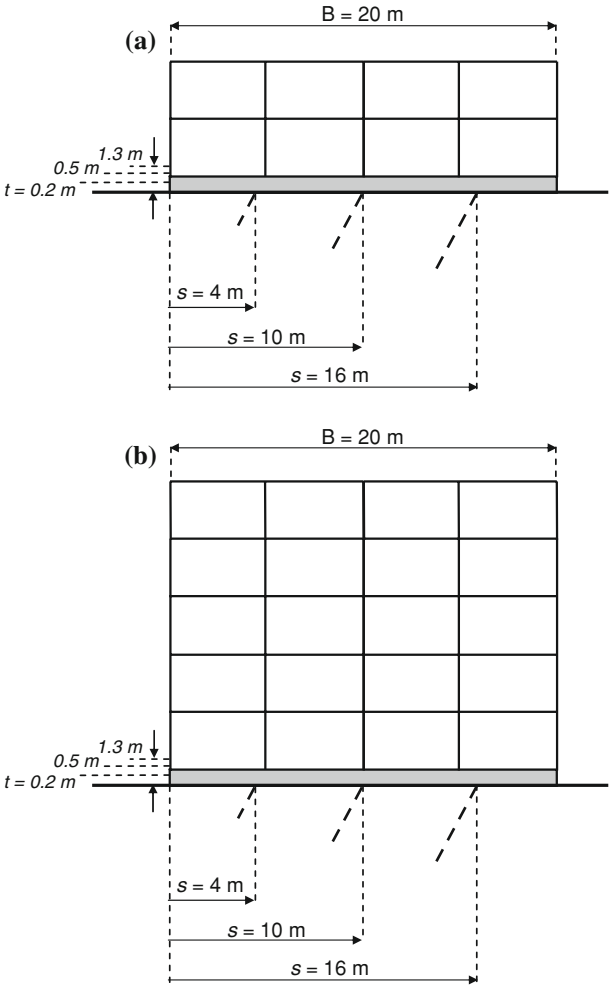

Fig. 19 Idealised structures of the parametric study: (**a**) 2-storey, $B = 20\,\text{m}$ building, and (**b**) 5-storey, $B = 20\,\text{m}$ building

($s/B = 0.2$, 0.5, and 0.8, respectively). The 18 idealised structures are illustrated in Fig. 19; their properties are summarised in Table 3.

Given the multitude of structure–foundation–position combinations to be analysed, a dip angle $a = 60^\circ$ has been selected for all of the analyses, considered typical for normal faults. To investigate the role of soil compliance, our idealised structures are analysed in conjunction with two idealised types of sand (Anastasopoulos et al. 2007):

- Dense Sand: $\varphi_p = 45^\circ$, $\varphi_{res} = 30^\circ$, $\psi_p = 18^\circ$, $\gamma_y = 0.015$, and $\gamma_f^P = 0.0516$
- Loose Sand: $\varphi_p = 32^\circ$, $\varphi_{res} = 30^\circ$, $\psi_p = 3^\circ$, $\gamma_y = 0.030$, and $\gamma_f^P = 0.0616$

The idealised dense sand is stiffer and reaches failure at relatively low strains ($\gamma_y = 1.5\%$). Hence, as demonstrated in Anastasopoulos et al. (2007), it exhibits "brittle" behaviour allowing for the rupture to outcrop at relatively small normalised bedrock displacement h/H. On

Table 3 Properties of the idealised structures of the parametric fault-foundation interaction study

Normalised distance s/B	Idealised sand type	Number of stories (#)	Raft thickness (m)	Foundation stiffness EI (kNm^2)	Equivalent dead load q (kN/m)
0.2	Dense	2	0.2	2.0×10^5	25.0
			0.5	3.1×10^6	32.5
			1.3	5.5×10^7	52.5
		5	0.2	2.0×10^5	55.0
			0.5	3.1×10^6	62.5
			1.3	5.5×10^7	82.5
	Loose	2	0.2	2.0×10^5	25.0
			0.5	3.1×10^6	32.5
			1.3	5.5×10^7	52.5
		5	0.2	2.0×10^5	55.0
			0.5	3.1×10^6	62.5
			1.3	5.5×10^7	82.5
0.5	Dense	2	0.2	2.0×10^5	25.0
			0.5	3.1×10^6	32.5
			1.3	5.5×10^7	52.5
		5	0.2	2.0×10^5	55.0
			0.5	3.1×10^6	62.5
			1.3	5.5×10^7	82.5
	Loose	2	0.2	2.0×10^5	25.0
			0.5	3.1×10^6	32.5
			1.3	5.5×10^7	52.5
		5	0.2	2.0×10^5	55.0
			0.5	3.1×10^6	62.5
			1.3	5.5×10^7	82.5
0.8	Dense	2	0.2	2.0×10^5	25.0
			0.5	3.1×10^6	32.5
			1.3	5.5×10^7	52.5
		5	0.2	2.0×10^5	55.0
			0.5	3.1×10^6	62.5
			1.3	5.5×10^7	82.5
	Loose	2	0.2	2.0×10^5	25.0
			0.5	3.1×10^6	32.5
			1.3	5.5×10^7	52.5
		5	0.2	2.0×10^5	55.0
			0.5	3.1×10^6	62.5
			1.3	5.5×10^7	82.5

the other hand, the idealised loose sand is more compliant and reaches failure at higher strain levels ($\gamma_y = 3\%$). It is therefore expected to exhibit more "ductile" behaviour, allowing for the rupture to delay its emergence.

5.2 Summary of results

The discussion of all of the results of the parametric study is clearly beyond the scope of this paper. Hence, a summary of the results is presented in the following sections, focusing on the effect of: (i) the distance s, (ii) the equivalent surcharge load q, and (iii) soil compliance

(dense versus loose sand). The effect of foundation stiffness has been investigated in more detail in Anastasopoulos et al. (2008), and shall not be repeated here.

The results are discussed in terms of deformed mesh with superimposed plastic shear strains, the soil vertical displacement profile Δy, and the contact pressure p along the foundation. In all cases the results are compared with the free-field to deduce the effect of FR-SFSI. The contact pressure is compared with its initial distribution ($h = 0$, before application of the dislocation) to reveal which parts of the structure are loosing contact with the bearing soil: foundation uplifting. The left part of the building that uplifts is denoted as u_L, the right u_R, and u if the uplifting takes place near the centre. Accordingly, the parts of the foundation that maintain contact with the soil are denoted as b_L and b_R, depending if it is at the left or right side of the building, and b if it is at the centre. The differential settlement of the foundation Dy is also reported to provide an estimate of the relative distress of each structure, mainly in terms of functionality. Finally, the maximum amplitude of bending moment of the superstructure, $M_{S,\max}$, and the foundation, $M_{F,\max}$, is also reported as a measure of structural distress.

5.2.1 Illustration of the effect of distance s

The effect of the position of the building relative to the unperturbed (free-field) fault rupture, as expressed through distance s, is illustrated in Fig. 20. We compare the response of the idealised 2-storey building resting on dense sand and founded through a $t = 0.5$ m raft foundation, positioned at $s = 4$ m and 16 m.

In the first case, the building is mainly resting on the footwall, not causing any significant diversion of the rupture path. The differential settlement does not exceed $\Delta y = 19$ cm, with the bending moment of foundation and superstructure reaching $M_{F,\max} = 1,547$ kNm and $M_{S,\max} = 735$ kNm, respectively. The stressing of the structure is mainly due to its detachment from the bearing soil: the building loses contact at both sides, $u_L = 6$ m, $u_R = 3$ m; with only its central part maintaining contact at a width $b = 11$ m. The two unsupported spans (u_R and u_L) essentially act as cantilevers on "elastic" supports, generating hogging deformation of the structure.

By moving the dislocation to $s = 16$ m, the interaction effects are altered significantly. The rupture is now divided in two separate branches. The right one diverts slightly towards the footwall by about 2 m, while the left is equally diverted towards the hanging wall (by about 3 m). A fault scarp is formed near the right edge of the building. As a consequence, the middle part of the building looses contact with the bearing soil, $u = 11$ m, while the left and right part of it are the ones that bear the load of the structure, $b_L = 2$ m and $b_R = 7$ m. While, the differential displacement reaches $\Delta y = 159$ cm, the bending moments are not increased accordingly: $M_{F,\max} = -1,354$ kNm and $M_{S,\max} = -995$ kNm. The structure is supported at its two edges (b_L and b_R), with its central detached span (u) acting as a "simply supported" beam on "elastic" supports. Now, the bending of the whole structure is to the opposite direction, i.e. sagging deformation (this is the reason for the negative sign in $M_{F,\max}$ and $M_{S,\max}$).

5.2.2 Illustration of the effect of surcharge load q

To illustrate the effect of the equivalent surcharge load q, we compare a 2-storey to a 5-storey building (Fig. 21). Both buildings are positioned at $s = 10$ m, resting on dense sand, and founded through a $t = 0.5$ m slab foundation.

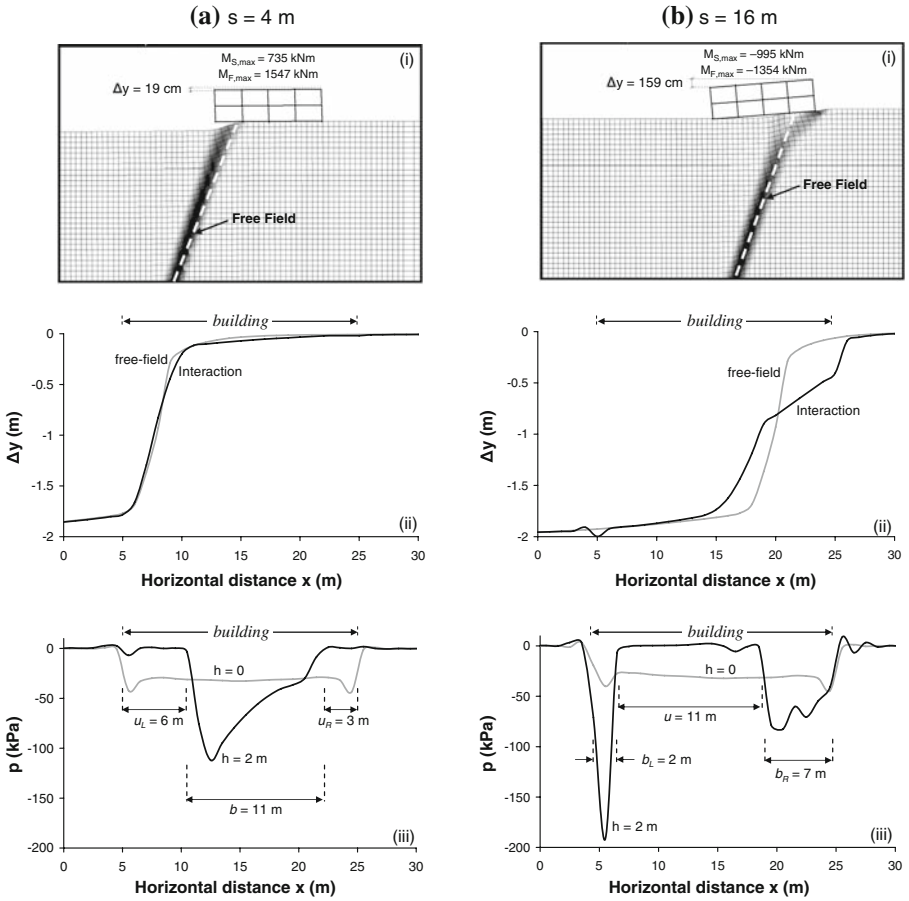

Fig. 20 Illustration of the effect of distance s: 2-storey, $B = 20\,\text{m}$ building with $t = 0.5\,\text{m}$ slab foundation on dense sand, and the fault rupture at (**a**) $s = 4\,\text{m}$, and (**b**) $s = 16\,\text{m}$; (i) Deformed mesh and plastic strain, (ii) Vertical displacement at the surface [The results of the interaction analysis (black line) are compared with the free-field (grey line) for $h = 2\,\text{m}$.], and (iii) contact stresses σ_v, [the grey line ($h = 0$) refers to the contact stresses before application of the dislocation]

In the case of the 2-storey structure ($q = 32.5\,\text{kPa}$), the rupture path is divided in two separate branches, but it is not diverted outside the limits of the structure. The left branch seems to be the major one, and diverts by about 2–3 m towards the hanging wall (to the left), but a distinct fault scarp outcrops beneath the building. The differential settlement reaches $\Delta y = 206\,\text{cm}$, with the building finding support at the left edge and close to the middle. From left to right, there is first a small section of the building, $b_L = 1\,\text{m}$, where contact is maintained, followed by an uplifted span, $u_L = 7\,\text{m}$, then a second support region close to the middle, $b_R = 6\,\text{m}$, and finally the far most right unsupported span, $u_R = 6\,\text{m}$. While the medium-left simply supported beam-type span (u_L) generates sagging deformation, the cantilever-type span (u_R) at the right is responsible for the opposite (i.e. hogging deformation), counterbalancing part of the downward bending due to u_L. The result is that the maximum moments are in the hogging sense ($M_{F,\max} = 1,870\,\text{kNm}$ and $M_{S,\max} = 1,094\,\text{kNm}$), due to the right-hand cantilever, u_R.

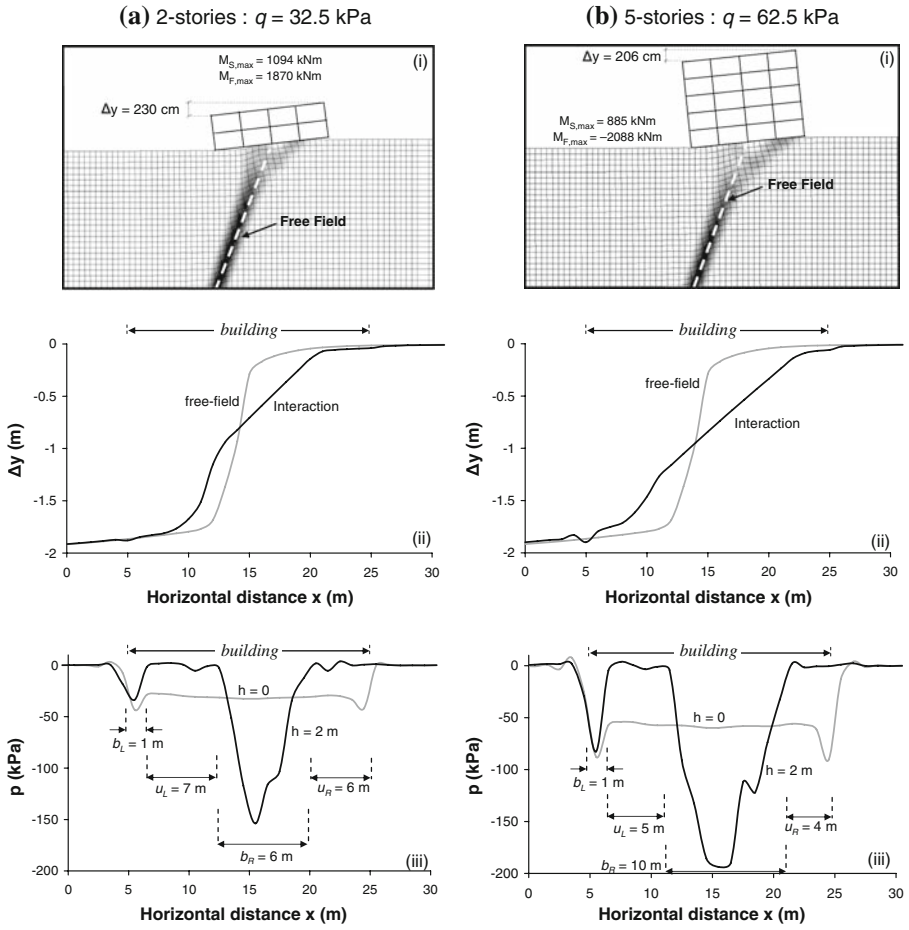

Fig. 21 Illustration of the effect of the equivalent surcharge load q: $B = 20$ m building, with $t = 0.5$ m slab foundation on dense sand, fault rupture at $s = 10$ m; (**a**) 2-storeys ($q = 32.5$ kPa), and (**b**) 5-storeys ($q = 62.5$ kPa); (i) Deformed mesh and plastic strain, (ii) Vertical displacement at the surface [The results of the interaction analysis (black line) are compared with the free-field (grey line) for $h = 2$ m.], and (iii) contact stresses σ_v, [the grey line ($h = 0$) refers to the contact stresses before application of the dislocation]

The response of the 5-storey structure ($q = 62.5$ kPa) is qualitatively the same, but due to the increased surcharge load the diversion of the rupture is more intense. The rupture path is again divided in two separate branches, with the left one diverting by about 3 m towards the hanging wall, and the right one about 6 m to the right (towards the footwall). As a result, the differential displacement is reduced to $\Delta y = 188$ cm. Besides from the larger diversion of the right branch of the rupture, the increase of q also leads to a decrease of the detached regions of the building: $b_L = 1$, $u_L = 5$, $b_R = 10$, and $u_R = 4$ m. The result is a reduction of $M_{S,\max}$ to 885 kNm, despite the fact that q is practically doubled. Notice also that $M_{F,\max}$ is now negative (sagging) and only marginally larger ($-2,088$ kNm). This indicates that the decrease of the simply supported beam-type span u_L (from 7 to 5 m) overshadows the effect of the decrease of the cantilever-type span u_R (from 6 to 4 m) so that there is a net (u_L-induced) sagging deformation.

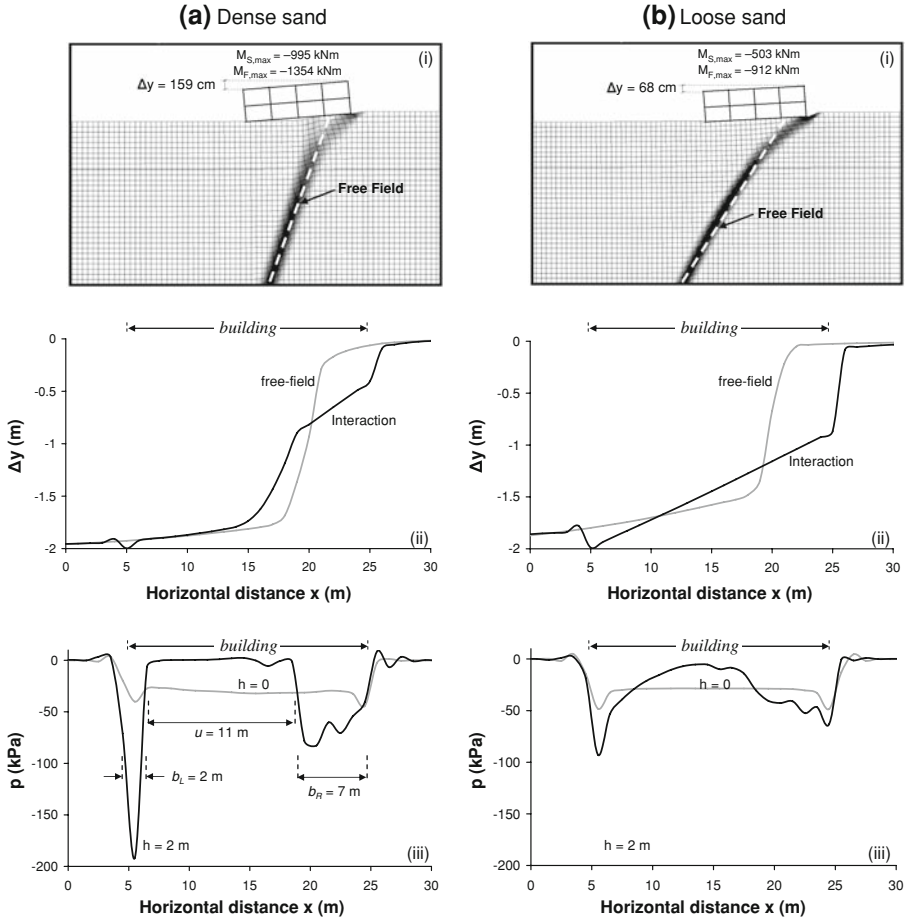

Fig. 22 Illustration of the effect of soil compliance: 2-storey, $B = 20\,\text{m}$ building, fault rupture at $s = 16\,\text{m}$, resting on $t = 0.5\,\text{m}$ raft foundation; (**a**) Dense sand, and (**b**) Loose sand; (i) Deformed mesh and plastic strain, (ii) Vertical displacement at the surface [The results of the interaction analysis (black line) are compared with the free-field (grey line) for $h = 2\,\text{m}$.], and (iii) contact stresses σ_v, [the grey line ($h = 0$) refers to the contact stresses before application of the dislocation]

5.2.3 Illustration of the effect of soil compliance

The effect of soil compliance is illustrated in Fig. 22. We compare the response of the idealised 2-storey building on $t = 0.5\,\text{m}$ slab foundation, and at $s = 16\,\text{m}$, resting on the idealised dense and loose sand.

Given that the first case has already been discussed, we mainly focus on the differences between the two types of sand. First of all, while in dense sand the fault rupture is divided in two separate branches, with the left of them outcropping beneath the structure, in the case of loose sand the rupture is clearly diverted to the right edge. As a result, the building maintains full contact, $b = 20\,\text{m}$, and the differential settlement is decreased substantially to $\Delta y = 68\,\text{cm}$ (compared to 159 cm). Equally significant is the decrease of the stressing of the structure: $M_{F,\max} = -912\,\text{kNm}$ and $M_{S,\max} = -503\,\text{kNm}$. It is noted, however, that even

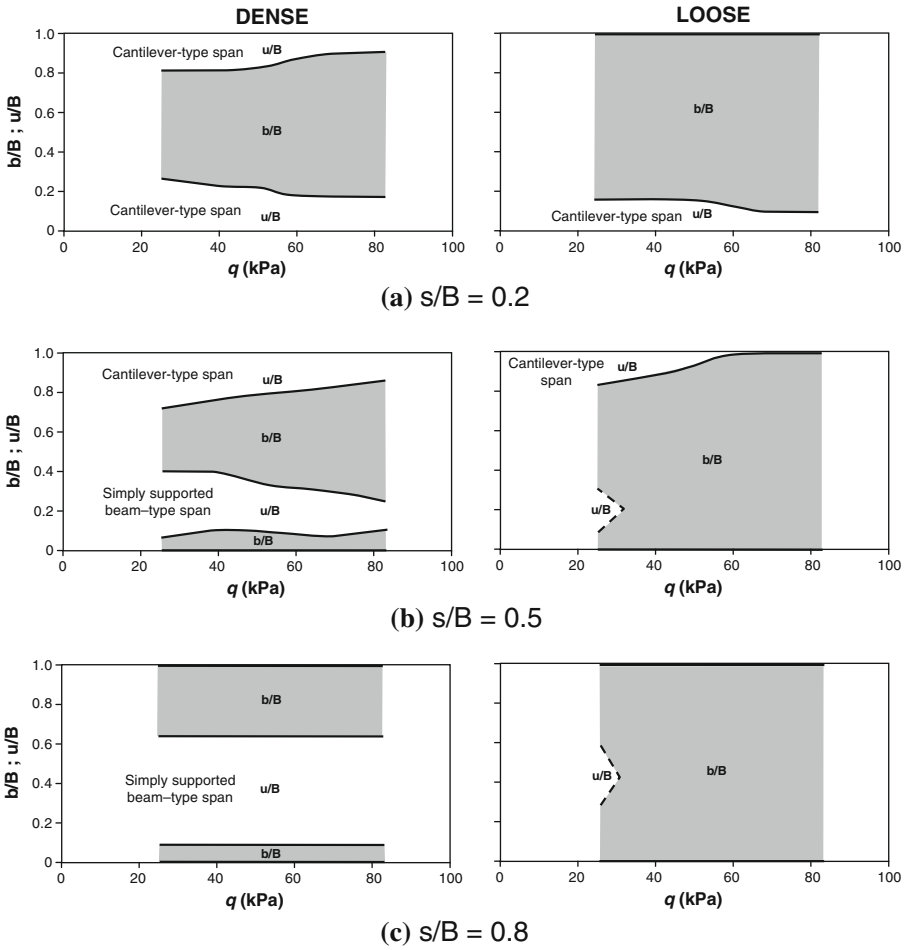

Fig. 23 Summary of analysis results illustrating the normalised (to the width B) uplifted, u/B, and effective, b/B, regions of the foundation with respect to the equivalent surcharge load q, and soil compliance for: (**a**) $s/B = 0.2$, (**b**) $s/B = 0.5$, and (**c**) $s/B = 0.8$. Results are plotted for $h = 2\,\text{m}$

without any detachment taking place, the structure is subjected to some noticeable stressing. The latter is attributable to the deformation of the soil mass supporting the building.

5.3 Synopsis

The results of the parametric study are summarised in Figs. 23 and 24. Emphasis is placed on the effect of the surcharge load q, soil compliance (dense versus loose sand), and the distance s.

Figure 23 illustrates the detached (unsupported), u, and effective, b, regions of the foundation with respect to the equivalent surcharge load q, and soil compliance for the three investigated locations relative to the free-field fault rupture ($s/B = 0.2$, 0.5, and 0.8). Both u and b are normalised to the width of the foundation B.

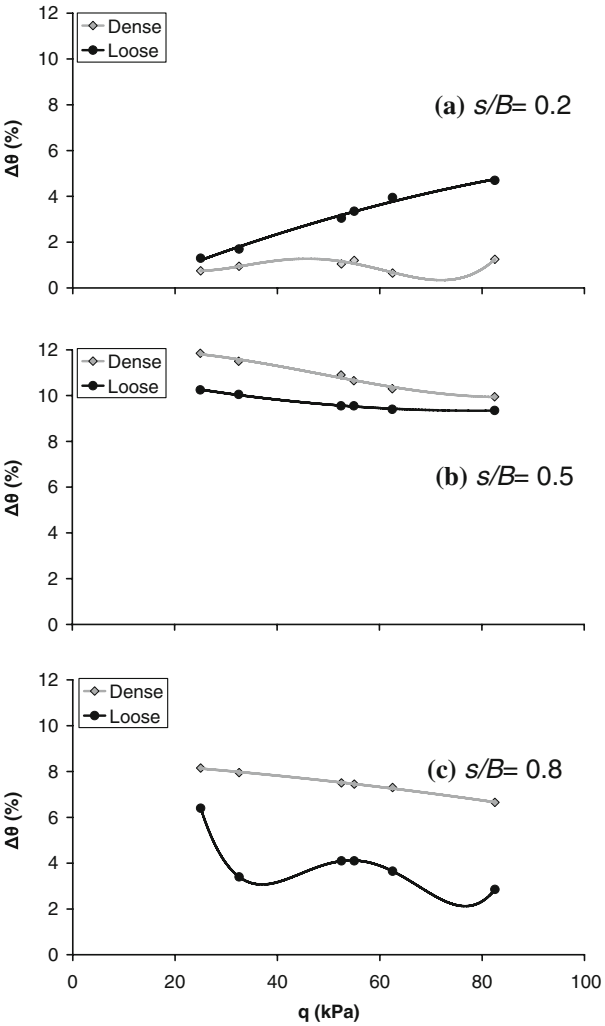

Fig. 24 Summary of analysis results illustrating the rotation $\Delta\theta$ of the structure with respect to the equivalent surcharge load q, and soil compliance for: (**a**) $s/B = 0.2$, (**b**) $s/B = 0.5$, and (**c**) $s/B = 0.8$. Results are plotted for $h = 2\,\text{m}$

In dense sand, for $s/B = 0.2$ the increase of q leads to an increase of the effective foundation width b/B from 0.6 to 0.75, reducing the maximum (unsupported) cantilever-type span from $u/B = 0.25$ to 0.20. Similarly, for $s/B = 0.5$ the increase of q leads to the decrease of the cantilever-type u/B from 0.25 to 0.20, and of the simply supported beam-type u/B from 0.30 to 0.25. In stark contrast, in the case of $s/B = 0.8$ the increase of q does not seem to play a significant role. In loose sand, for $s/B = 0.2$ the increase of q limits the maximum cantilever-type u/B to 0.10 instead of 0.15. For $s/B = 0.5$ and 0.8, the increase of q leads to full contact: $b/B \rightarrow 1.0$.

Figure 24 depicts the rotation of the foundation $\Delta\theta$, with respect to q, s/B, and soil compliance, for $h = 2\,\text{m}$. When the rupture outcrops close to the left edge of the foundation, $s/B = 0.2$, the increase of q leads to significant increase of $\Delta\theta$ in the case of loose sand, but practically no increase at all in dense sand. Soil compliance can clearly be seen to act unfavorably with respect to foundation rotation: $\Delta\theta$ is larger in loose sand. In contrast, for

$s/B = 0.5$ (i.e. the dislocation outcrops at the middle of the structure), the increase of q has a less pronounced effect on $\Delta\theta$ for both types of sand. In addition, soil compliance is now beneficial with respect to $\Delta\theta$ (i.e. the foundation rotation is reduced with the loose sand). Finally, when the rupture emerges close to the right edge of the foundation, $s/B = 0.8$, the increase of q leads to a significant decrease of $\Delta\theta$ for both sands. Soil compliance is again beneficial in terms of $\Delta\theta$.

6 Conclusions

In this paper three different numerical modelling approaches were employed to analyse fault rupture propagation and its interaction with overlying structures. The three analysis methods were validated against a series of centrifuge model tests conducted at the University of Dundee. The comparisons have shown that reliable predictions can be achieved not only with reasonably sophisticated constitutive soil models taking account of strain softening, but—in several cases—also with standard models, provided adequately refined FE meshes are used, as well as interface elements with tension cut-off between the soil and the structure.

Having validated the numerical simulation approaches, Method 2 was utilised to conduct a short parametric study of idealised 2- and 5-storey residential structures lying on slab foundations. The main conclusions are as follows:

[1] The increase of the equivalent surcharge load q leads to an increase of the stress change beneath the foundation, intensifying the diversion of the rupture path. The dislocation *"finds it easier"* to propagate by rupturing the soil with the lowest strength. Therefore, since the soil beneath the building is of enhanced strength, thanks to the additional stress increase provided by the bearing pressure q, the rupture bends to avoid this zone beneath the structure.

[2] An additional favorable effect of the increase of q lies on the "smoothing" of the settlement profile. With a larger surcharge load, and provided that the foundation is continuous and adequately rigid, the deforming soil is forced to comply with the kinematics of the foundation, leading to a decrease of the detached regions of the foundation. The latter are mainly responsible for the stressing of the structure, and hence their decrease is beneficial.

[3] The increase of soil compliance is always beneficial for the response of the investigated structures. Structures on loose sand experience far less separation and uplifting than the ones lying on dense sand. The fault rupture may be more intensely diverted in dense sand, but the increased compliance of loose sand leads to significant diffusion of the rupture beneath the foundation.

[4] The rotation $\Delta\theta$ of the structure (for given soil depth H and imposed dislocation h) is a function of: (a) the relative location to the free-field fault rupture, expressed through s in our analysis; (b) the surcharge load q; and (c) soil compliance. In general, $\Delta\theta$ is maximised when the rupture outcrops close to middle of the foundation ($s/B = 0.5$); it is minimised when the rupture emerges near the edge of the structure that is closest to the hanging wall ($s/B = 0.2$). In terms of foundation rotation, the increase of soil compliance is detrimental for $s/B = 0.2$, but beneficial for all other cases investigated herein.

Acknowledgements This work formed part of the EU research project "*QUAKER*" which is funded through the EU Fifth Framework Programme: Environment, Energy, and Sustainable Development, Research and

Technological Development Activity of Generic Nature: the Fight against Natural and Technological Hazards, under contract number: EVG1-CT-2002-00064.

References

ABAQUS Inc. (2004) ABAQUS V.6.4 user's manual. Providence, Rhode Island, USA

Anastasopoulos I (2005) Fault rupture–soil–foundation–structure interaction. Ph.D. Dissertation, School of Civil Engineering, National Technical University, Athens, 570 pp

Anastasopoulos I, Gazetas G (2007a) Foundation-structure systems over a rupturing normal fault: part I. Observations after the Kocaeli 1999 earthquake. Bull Earthq Eng 5(3):253–275

Anastasopoulos I, Gazetas G (2007b) Behaviour of structure–foundation systems over a rupturing normal fault: part II. Analysis of the Kocaeli case histories. Bull Earthq Eng 5(3):277–301

Anastasopoulos I, Gazetas G, Bransby MF, Davies MCR, El Nahas A (2007) Fault rupture propagation through sand: finite element analysis and validation through centrifuge experiments. J Geotech Geoenviron Eng ASCE 133(8):943–958

Anastasopoulos I, Gazetas G, Bransby MF, Davies MCR, El Nahas A (2008) Normal fault rupture interaction with strip foundations. J Geotech Geoenviron Eng ASCE 134 (in print)

Berill JB (1983) Two-dimensional analysis of the effect of fault rupture on buildings with shallow foundations. Soil Dyn Earthq Eng 2(3):156–160

Bransby MF, Davies MCR, El Nahas A (2008a) Centrifuge modelling of normal fault-foundation interaction. Bull Earthq Eng, special issue: Integrated approach to fault rupture- and soil-foundation interaction. doi:10.1007/s10518-008-9079-0

Bransby MF, Davies MCR, El Nahas A (2008b) Centrifuge modelling of reverse fault-foundation interaction. Bull Earthq Eng, special issue: Integrated approach to fault rupture- and soil-foundation interaction. doi:10.1007/s10518-008-9080-7

Bray JD (1990) The effects of tectonic movements on stresses and deformations in earth embankments. Ph.D. Dissertation, University of California, Berkeley

Bray JD (2001) Developing mitigation measures for the hazards associated with earthquake surface fault rupture. In: Workshop on seismic fault-induced failures—possible remedies for damage to urban facilities. University of Tokyo Press, pp 55–79

Bray JD, Seed RB, Cluff LS, Seed HB (1994a) Earthquake fault rupture propagation through soil. J Geotech Eng ASCE 120(3):543–561

Bray JD, Seed RB, Seed HB (1994b) Analysis of earthquake fault rupture propagation through cohesive soil. J Geotech Eng ASCE 120(3):562–580

Cole DAJr., Lade PV (1984) Influence zones in alluvium over dip-slip faults. J Geotech Eng ASCE 110(5):599–615

Duncan JM, Lefebvre G (1973) Earth pressure on structures due to fault movement. J Soil Mech Found Eng ASCE 99:1153–1163

Erdik M (2001) Report on 1999 Kocaeli and Düzce (Turkey) earthquakes. In: Casciati F, Magonette G (eds) Structural control for civil and infrastructure engineering. World Scientific

Erickson SG, Staryer LM, Suppe J (2001) Initiation and reactivation of faults during movement over a thrust-fault ramp: numerical mechanical models. J Struct Geol 23:11–23

Faccioli E, Anastasopoulos I, Gazetas G, Callerio A, Paolucci R (2008) Fault rupture-foundation interaction: selected case histories. Bull Earthq Eng, special issue: Integrated approach to fault rupture- and soil-foundation interaction doi:10.1007/s10518-008-9089-y

Gaudin C (2002) Experimental and theoretical study of the behaviour of supporting walls: validation of design methods. Ph.D. Dissertation, Laboratoire Central des Ponts et Chaussées, Nantes, France

Gerolymos N, Vardoulakis I, Gazetas G (2007) A Thermo-poro–viscoplastic shear band model for seismic triggering and evolution of catastrophic landslides. Soils Found 47(1):11–25

Griffiths DV, Prévost JH (1990) Stress strain curve generation from simple triaxial parameters. Int J Numer Anal Methods Geomech 14(8):587–594

Hayashi H, Honda M, Yamada T, Tatsuoka F (1992) Modeling of nonlinear stress strain relations of sands for dynamic response analysis. In: Proceedings, 10th WCEE, Madrid, Spain, vol 11, pp 6819–6825

Iwan WD (1967) On a class of models for the yielding behavior of continuous and composite systems. J Appl Mech Trans ASME 34(E3):612–617

Jewell RA, Roth CP (1987) Direct shear tests on reinforced sand. Géotechnique 37(1):53–68

Lade PV (1987) Behaviour and plasticity theory for metals and frictional materials. In: Proceedings 2nd international conference on constitutive laws for engineering materials, Tuscon, Arizona, pp 327–334

Lade PV, Cole DAJr., Cummings D (1984) Multiple failure surfaces over dip-slip faults. J Geotech Eng ASCE 110(5):616–627

Loukidis D (1999) Active fault propagation through soil. Diploma Thesis, School of Civil Engineering, National Technical University, Athens

Loukidis D, Bouckovalas G (2001) Numerical simulation of active fault rupture propagation through dry soil. In: Proceedings 4th international conference on recent advances in geotechnical earthquake engineering and soil dynamics and symposium in honor of Professor W.D. Liam Finn, San Diego, CA, March, pp 26–31

Mróz A (1967) On the description of anisotropic work hardening. J Mech Phys Solids 15:163–175

Muir Wood D (2002) Some observations of volumetric instabilities in soils. Int J Solids Struct 39:3429–3449

Muir Wood D, Stone KJL (1994) Some observations of zones of localisation in model tests on dry sand. In: Chambon R, Desrues J, Vardoulakis I (eds) Localisation and bifurcation theory for soils and rocks. A.A. Balkema, Rotterdam, pp 155–164

Niccum MR, Cluff LS, Chamoro F, Wylie L (1976) Banco Central de Nicaragua: a case history of a high-rise building that survived surface fault rupture. In: Humphrey CB (ed) Engineering geology and soils engineering symposium, no. 14. Idaho Transportation Department, Division of Highways, pp 133–144

Pamuk A, Kalkanb E, Linga HI (2005) Structural and geotechnical impacts of surface rupture on highway structures during recent earthquakes in Turkey. Soil Dyn Earthq Eng 25:581–589

PLAXIS (2006) Finite element code for soil and rock analyses, users manual, by R.B.J. Brinkgreve, Rotterdam, Balkema, 2002

Popescu R (1995) Stochastic variability of soil properties: data analysis, digital simulation, effects on system behavior. Ph.D. Thesis, Princeton University

Popescu R, Prevost JH (1995) Comparison between VELACS numerical "Class A" predictions and centrifuge experimental soil test results. Int J Soil Dyn Earthq Eng 14:76–92

Potts DM, Dounias GT, Vaughan PR (1990) Finite element analysis of progressive failure of Carsington Embankment. Géotechnique 40(1):79–101

Potts DM, Kovacevic N, Vaughan PR (1997) Delayed collapse of cut slopes in stiff clay. Géotechnique 47(5):953–982

Prevost JH (1977) Mathematical modeling of monotonic and cyclic undrained clay behavior. Int J Numer Methods Geomech 1(2):195–216

Prevost JH (1981) DYNAFLOW: a nonlinear transient finite element analysis program. Technical report, Department of Civil Engineering and Operations Research, Princeton University

Prevost JH (1985) A simple plasticity theory for frictional cohesionless soils. Soil Dyn Earthq Eng 4:9–17

Prevost JH (1989) DYNA1D a computer program for nonlinear seismic site response analysis. Technical Documentation NCEER-89-0025. Technical report, Department of Civil Engineering and Operations Research, Princeton University

Prevost JH (1993) Nonlinear dynamic response analysis of soil and soil-structure interacting systems. In: Proceedings seminar on soil dynamics and geotechnical earthquake engineering, Lisboa, Portugal, Balkema, Rotterdam, pp 49–126

Roth WH, Scott RF, Austin I (1981) Centrifuge modelling of fault propagation through alluvial soils. Geophys Res Lett 8(6):561–564

Roth WH, Sweet J, Goodman RE (1982) Numerical and physical modelling of flexural Slip phenomena and potential for fault movement. Rock Mech 12:27–46 (Suppl.)

Shibuya S, Mitachi T, Tamate S (1997) Interpretation of direct shear box testing of sands as quasi-simple shear. Géotechnique 47(4):769–790

Stone KJL, Muir Wood D (1992) Effects of dilatancy and particle size observed in model tests on sand. Soils Found 32(4):43–57

Ulusay R, Aydan O, Hamada M (2002) The behaviour of structures built on active fault zones: examples from the recent earthquakes of Turkey. Struct Eng Earthq Eng JSCE 19(2):149–167

Ural D (2001) The 1999 Kocaeli and Duzce earthquakes: lessons learned and possible remedies to minimize future Losses. In: Konagai K (ed) Proceedings workshop on seismic Fault induced failures, Tokyo, Japan

White DJ, Take WA, Bolton MD (2003) Soil deformation measurement using particle image velocimetry (PIV) and photogrammetry. Géotechnique 53(7):619–631

Youd TL (1989) Ground failure damage to buildings during earthquakes. In: Foundation engineering—current principles and practices, New York: ASCE 1:758–770

Youd TL, Bardet J-P, Bray JD (2000) Kocaeli, Turkey, earthquake of August 17, 1999 Reconnaissance Report, Earthquake Spectra, Suppl. A to vol 16, 456 pp